PNAS RESEARCH ARTICLE | PLANT BIOLOGY

Ca^{2+}-dependent phosphorylation of NRAMP1 by CPK21 and CPK23 facilitates manganese uptake and homeostasis in *Arabidopsis*

Dali Fu[a,b,1], Zhenqian Zhang[a,1], Lukas Wallrad[c,1], Zhangqing Wang[a], Stefanie Höller[d], ChuanFeng Ju[a], Ina Schmitz-Thom[c], Panpan Huang[a], Lei Wang[b], Edgar Peiter[d], Jörg Kudla[c,2], and Cun Wang[a,2]

Edited by Mary Lou Guerinot, Dartmouth College, Hanover, NH; received March 15, 2022; accepted September 2, 2022

Homeostasis of the essential micronutrient manganese (Mn) is crucially determined through availability and uptake efficiency in all organisms. Mn deficiency of plants especially occurs in alkaline and calcareous soils, seriously restricting crop yield. However, the mechanisms underlying the sensing and signaling of Mn availability and conferring regulation of Mn uptake await elucidation. Here, we uncover that Mn depletion triggers spatiotemporally defined long-lasting Ca^{2+} oscillations in *Arabidopsis* roots. These Ca^{2+} signals initiate in individual cells, expand, and intensify intercellularly to transform into higher-order multicellular oscillations. Furthermore, through an interaction screen we identified the Ca^{2+}-dependent protein kinases CPK21 and CPK23 as Ca^{2+} signal-decoding components that bring about translation of these signals into regulation of uptake activity of the high-affinity Mn transporter natural resistance associated macrophage proteins 1 (NRAMP1). Accordingly, a *cpk21/23* double mutant displays impaired growth and root development under Mn-limiting conditions, while kinase overexpression confers enhanced tolerance to low Mn supply to plants. In addition, we define Thr498 phosphorylation within NRAMP1 as a pivot mechanistically determining NRAMP1 activity, as revealed by biochemical assays and complementation of yeast Mn uptake and *Arabidopsis nramp1* mutants. Collectively, these findings delineate the Ca^{2+}-CPK21/23-NRAMP1 axis as key for mounting plant Mn homeostasis.

Manganese | Ca^{2+}-NRAMP1 | CPK21/23-Arabidopsis

Significance

Manganese (Mn) deficiency represents a serious and widespread disturbance of crop nutrition in alkaline and calcareous soils. However, it has remained largely unknown how fluctuations in Mn supply are sensed and signaled and how the activity of Mn transporters is regulated. Here we discovered that Mn depletion triggers spatiotemporally defined multicellular Ca^{2+} oscillations in a specific "low Mn-sensing niche" in *Arabidopsis* roots. We identified the Ca^{2+} signal-decoding kinases CPK21 and CPK23 as regulating the Mn uptake transporter NRAMP1. We defined Thr498 in NRAMP1 as a target of both kinases and as a pivot mechanistically determining NRAMP1 activity. These findings delineate a Ca^{2+}-CPK21/23-NRAMP1 axis as key mechanism for establishing plant resilience to limited Mn supply.

Manganese (Mn) is an essential micronutrient for all organisms and a crucial regulator of manifold cellular processes. It serves as an essential dietary and nutrient element in animals and plants and is important for the activity of many metalloproteins in all kingdoms of life (1–4). Most important, factors affecting the availability of Mn in the rhizosphere are its pH and redox potential. At present, Mn deficiency is a serious and widespread crop nutritional disorder in alkaline soils, as well as in calcareous soils with elevated pH, where the bioavailability of Mn can decrease far below the level that is required for normal plant growth and development (3, 5).

Organismic Mn homeostasis of plants results from a complex interplay of Mn uptake into roots, interorgan distribution, and allocation (3). In addition, cellular Mn uptake and homeostasis are faithfully balanced through storage and release of Mn in organelles like the vacuole and the Golgi. Many components that confer the hardwiring of cellular and organismic Mn homeostasis in plants are known (3). Mn uptake and distribution in plants depend on a variety of Mn transporters, including natural resistance associated macrophage proteins (NRAMP) (6–11), cation exchangers (CAX) (12–14), vacuolar iron transporters (VIT) (15, 16), ZRT/IRT-related proteins (ZIP) (17, 18), cation diffusion facilitator/metal tolerance proteins (CDF/MTP) (19–22), endoplasmic reticular-type calcium ATPases (ECA) (23–25), yellow stripe-like proteins (YSL) (26–28), BICAT1/PAM71, PML3, and BICAT2/CMT1 (members of the Unknown Protein Family, UPF0016) (29–32). These Mn transporters are located at different subcellular compartments and are involved in the distribution of Mn and in responses to fluctuating environmental Mn supply (3, 33).

In *Arabidopsis*, as in all higher plants, Ca^{2+} signals are decoded and translated into target protein phosphorylation by two complex signaling networks, the 34-member family of Ca^{2+}-dependent protein kinases (CPKs) and the CBL-CIPK network formed through specific complex formation of 10 calcineurin-B–like Ca^{2+} sensor proteins (CBLs) with distinct kinases of the 26-member CBL-interacting protein kinase (CIPK) family (34–36). Most recently, a crucial role of Ca^{2+} signaling and Ca^{2+}-dependent phosphorylation in regulating vacuolar Mn sequestration and release has been discovered in *Arabidopsis* (37–40). It was reported that exposure to excess Mn triggers rapid

Author contributions: C.W. designed research; D.F., Z.Z., L. Wallrad, Z.W., S.H., C.J., I.S.-T., and P.H. performed research; D.F., Z.Z., and L. Wallrad analyzed data; and L. Wang, E.P., J.K., and C.W. wrote the paper.

The authors declare no competing interest.

This article is a PNAS Direct Submission.

[1]D.F., Z.Z., and L. Wallrad contributed equally to this work.

[2]To whom correspondence may be addressed. Email: cunwang@nwafu.edu.cn or jkudla@uni-muenster.de.

This article contains supporting information online at http://www.pnas.org/lookup/suppl/doi:10.1073/pnas.2204574119/-/DCSupplemental.

Published September 26, 2022.

and transient Ca^{2+} signals in *Arabidopsis* plants (37). Moreover, it was revealed that four Ca^{2+}-dependent protein kinases, CPK4/5/6/11, phosphorylate and activate the tonoplast-localized Mn transporter MTP8, protecting plants from high Mn (HMn) toxicity (37). Interestingly, the two CLB proteins CBL2/3 and their interacting kinases CIPK3/9/26 were subsequently also identified to phosphorylate MTP8 (38). However, in this case, CBL-CIPK–mediated phosphorylation of MTP8 caused its deactivation.

However, the signaling events and regulatory mechanisms conferring plant tolerance to limiting Mn supply so far wait to be uncovered. This is especially true for the components and mechanisms regulating cellular and organismic Mn uptake, which represent the prerequisite for all other subsequent facets of sustaining Mn homeostasis and have so far remained largely elusive. In *Arabidopsis*, Mn acquisition by the root, especially in Mn limiting conditions, is mainly mediated by the high-affinity plasma membrane-localized transporter NRAMP1, with some contribution of IRT1 (41). Accordingly, NRAMP1 function has been found to be essential for plant tolerance to low Mn (LMn) stress (4). With regard to NRAMP1 regulation, modulation of its subcellular localization and plasma membrane association through interaction with the pleckstrin homology domain-containing protein AtPH1 and through phosphorylation of Ser20, -22, and -24 in its N terminus have recently been reported (42, 43). However, the identity of kinases potentially conferring these and other aspects of NRAMP1 regulation have remained unknown.

Here, we report the surprising discovery that Mn depletion triggers a pattern of long-lasting multicellular Ca^{2+} oscillations, whose maximum is spatially confined to a specific cell group of the root elongation zone (EZ) that forms a low Mn-sensing niche (LMnSN). Through an interaction screen we identified CPK21 and CPK23 as Ca^{2+} signal-decoding components that likely bring about translation of these signals into regulation of NRAMP1 Mn uptake activity. Accordingly, *cpk21/23* mutants display impaired growth and root development under Mn-limiting conditions, while kinase overexpression confers enhanced tolerance to LMn supply to plants. We identify Ser20 and Thr498 within NRAMP1 as targets of both kinases and as pivots mechanistically determining NRAMP1 activity as evidenced by biochemical assays and complementation of LMn-sensitive yeast strains and *nramp1 Arabidopsis* mutants. Collectively, these findings delineate a Ca^{2+}-CPK21/23-NRAMP1 axis as key mechanism for establishing plant resilience to limited Mn supply and reveal how plants mechanistically initiate and mount their adaptation response to Mn micronutrient deprivation.

Results

Mn Depletion Specifically Causes a Complex Oscillatory Ca^{2+} Signaling Pattern Emanating in the EZ of Roots. During recent years, accumulating evidence supported a central role of Ca^{2+}-dependent phosphorylation processes in plant signaling and response reactions to fluctuating nutrient supply (44). However, it remained largely unresolved if fluctuating nutrient supply would cause discernable Ca^{2+} signals that would trigger activation of such phosphorylation cascades. This also holds true for Mn, although most recently the occurrence of rapid HMn-induced Ca^{2+} signals in *Arabidopsis* seedlings was reported (37). However, these aequorin-based investigations could only provide rather limited spatiotemporal resolution of these Ca^{2+} signals. We therefore sought to approach this enigma in our understanding of plant Mn signal transduction by using the recently developed ultrasensitive ratiometric Ca^{2+} reporter protein GCaMP6f-mCherry as a tool and *Arabidopsis* roots as a model system (45).

We first investigated the short-term response of *Arabidopsis* roots expressing GCaMP6f-mCherry under control of the constitutive UBQ10 promoter. To this end, we devised a custom-built flow-through chamber system mounted on an inverse microscope and comparatively studied the potential Ca^{2+} dynamics of roots in response to elevated Mn concentrations (HMn; 1.5 mM), Mn depletion (LMn; 0 μM), or in control conditions (NMn; Hoagland medium containing 20 μM Mn) for 1,800 s (30 min). Data points were acquired every 6 s and the $GFP^{em}/mCherry^{em}$ ratio was calculated and transformed into false-color depiction or graphical representation of relative ratio changes ($\Delta R/R_0$), respectively (Fig. 1 *A* and *B* and Movies S1–S3). In all three measurement regimes, we observed regular Ca^{2+} fluctuations in the meristem/root cap region, which are associated with normal root growth. Beyond that, we did not identify clearly discernable Ca^{2+} elevations in roots exposed to NMn and LMn. However, exposure of roots to HMn triggered a spatially defined Ca^{2+} signal restricted to the outer cell groups of the root EZ. We therefore defined a region of interest for representative cells of the EZ and performed detailed time-lapse measurements (Fig. 1*B*). These analyses revealed the occurrence of a transient Ca^{2+} signal starting to rise after approximately 1,020 s (17 min) after exposure to HMn that reached a maximum around 1,100 s (18 min) and subsequently declined. These results further corroborated the previously reported occurrence of Ca^{2+} signals in *Arabidopsis* in response to HMn and expanded these findings in that they established this pattern of Ca^{2+} signals as occurring specifically only in response to Mn elevation. Importantly, these findings also identified this HMn-specific Ca^{2+} signal as occurring in the EZ and exhibiting its maximum exclusively in the cortex cell layer of the EZ, and therefore define this specific group of cells as an "HMn-sensing niche" (HMnSN). However, these studies did not reveal any fast-occurring Ca^{2+} signal upon Mn depletion.

We therefore expanded the duration of our Ca^{2+} imaging analyses to 6 h with a data-acquisition interval of 2 min to minimize GCaMP6f-mCherry bleaching. Strikingly, this approach discovered the occurrence of oscillatory Ca^{2+} signals specifically in response to LMn exposure (Fig. 1 *C* and *D* and Movies S4–S6). These Ca^{2+} oscillations initiated 126 min (±4 min) after onset of Mn depletion and continued throughout the measurement period. These repetitive rises in cytoplasmic Ca^{2+} concentration exhibited a frequency of 31 (±6 min) and an average amplitude of 0.14 $\Delta R/R_0$ (±0.04). We did not detect any tendency for changes in amplitude or duration of individual oscillations over the measurement time (*SI Appendix*, Fig. S1 *A* and *B*). Spatially, these Ca^{2+} oscillations were centered in the EZ (Fig. 1*C*). Detailed inspection of Ca^{2+} oscillation formation by high-resolution microscopy revealed that in regard to its longitudinal, developmental dimension, each individual oscillation initiated centrally within the EZ and subsequently, within 15 min, expanded into the adjacent cell layers of the meristematic (MZ) and differentiation (DZ) zones. The subsequent signal decline occurred in the opposite direction. We also observed a remarkable differentiation of oscillation signal formation with regard to its transversal—cell type/layer-specific—dimension (Fig. 1*E* and *SI Appendix*, Fig. S1 *C* and *D*). Each oscillation initiated in the epidermis, expanded within 5 min into the cortex, and exhibited a vast intensity boost after it appeared in the stele. The longitudinal emanation of the Ca^{2+} oscillation, including its expansion into MZ and DZ, followed this stelar signal boost. Again, the transversal Ca^{2+} signal retrogression started in the stelar cell files and proceeded outwards.

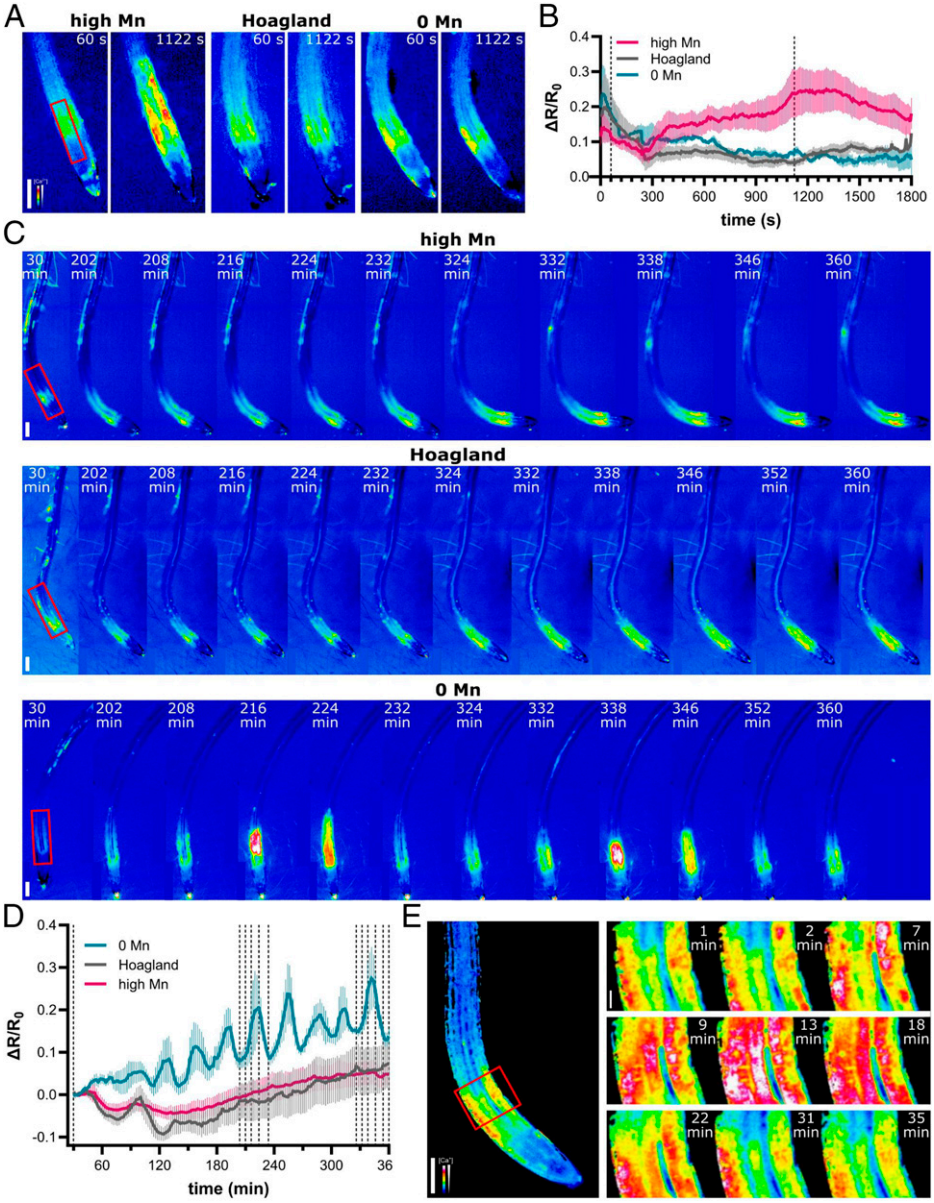

Fig. 1. Excess manganese and manganese depletion cause specific Ca^{2+} signaling pattern emanating in the EZ of *Arabidopsis* roots. (*A*) False color representation of cytoplasmic Ca^{2+} concentration at selected time points after exposure to HMn (1.5 mM Mn), control (Hoagland), or 0 Mn conditions. (Scale bar, 200 μm.) (*B*) Quantitative determination of cytoplasmic Ca^{2+} dynamics in response to varying Mn concentrations in the region of interest depicted in *A* (outer cell groups of the EZ). Mean and SEM; n = 6, 4, 3 (HMn, Hoagland, 0 Mn). (*C*) False color representation of cytoplasmic Ca^{2+} concentration in *Arabidopsis* roots at selected time points after onset of exposure to HMn, Hoagland, or 0 Mn. (Scale bar, 200 μm.) (*D*) Quantitative determination of cytoplasmic Ca^{2+} dynamics in the region of interest depicted in *C* (EZ and early DZ). Mean and SEM; n = 5, 8, 5 (HMn, Hoagland, 0 Mn). (*E*) High-resolution imaging of Ca^{2+} dynamics in selected cells of the EZ (red box) of an *Arabidopsis* root exposed to 0 Mn. Selected time points of one representative oscillation lasting for 35 min are depicted. (Scale bar, 200 μm.)

In summary, these findings reveal that plant exposure to LMn specifically triggers long-lasting multicellular Ca^{2+} oscillations in the EZ. The temporal and spatial order of events in this root domain conferring the formation of these Ca^{2+} oscillations functionally define this cell group as forming an LMnSN. Within this LMnSN the directed, stepwise, and subsequent intercellular spreading of Ca^{2+} signal amplitude formation (and regression) argues for underlying cell-to-cell mechanisms of signal transmission and formation, the combined function of which forms this complex multicellular signaling unit to create the observed Ca^{2+} oscillations.

The Ca^{2+}-Activated Kinases CPK21 and CPK23 Interact with the Mn Uptake Transporter NRAMP1 and Confer Plant Tolerance to Mn Deficiency. Having established that Mn depletion triggers a complex and oscillating Ca^{2+} signal pattern in roots, we next sought to identify the components that potentially decode this signal for triggering the consequently required adaptive adjustment of high-affinity Mn uptake through the NRAMP1 Mn transporter. CPKs are versatile sensor-responders translating Ca^{2+} signals into phosphorylation-mediated regulation of effector proteins (46, 47). We therefore devised an in vivo protein–protein interaction screen based on bimolecular fluorescence complementation (BiFC) that combined NRAMP1 with all 34 CPKs through coexpression of specific pairwise combinations in *Nicotiana benthamiana* leaves (*SI Appendix*, Fig. S2). Quantification of fluorescence as a consequence of BiFC that is indicative for efficient protein–protein interaction identified CPK21 and CPK23 as exhibiting most pronounced interaction with the Mn transporter. We moreover detected potential interaction of NRAMP1 with CPK4, CPK5, CPK6, and CPK11, although in these cases the fluorescence only reached approximately 50% of the intensity caused by the coexpression of CPK21 or CPK23 with NRAMP1.

In order to ascertain the physiological relevance of the identified potential CPK–NRAMP1 interactions, we analyzed the low-Mn tolerance of a suite of *cpk* mutants and mutant combinations. To this end, we obtained individual *cpk21* (SALK_043765) and *cpk23* (SALK_007958) mutants. Moreover, we generated a *cpk21/23* double mutant by introducing a CPK23 loss-of-function allele in *cpk21* through CRISPR/Cas-mediated mutagenesis. We subsequently characterized these mutants together with a

recently reported *cpk4/5/6/11* quadruple mutant, as well as *nramp1* and WT plants, which served as phenotype references, in low-Mn tolerance assays (Fig. 2 and *SI Appendix*, Fig. S3) (37). Scoring of root length, fresh weight, and root/shoot Mn accumulation did not reveal significant differences between WT and individual *cpk21* and *cpk23* mutants in both Mn-sufficient and Mn-deficient growth conditions. Similarly, we did not detect discernable phenotypic differences between *cpk4/5/6/11* and WT (*SI Appendix*, Fig. S3).

In sharp contrast, *cpk21/23* double mutant plants displayed an approximately 20% reduction of root length and an approximately 50% reduction of fresh weight, specifically only under Mn-deficient growth conditions as compared to WT (Fig. 2). While *nramp1* exhibited a similar fresh weight reduction upon Mn depletion as *cpk21/23*, root growth of *nramp1* was more severely affected (approximately 40%) than that of the kinase double mutant. Moreover, Mn deficiency affected the Mn concentration specifically in the shoot, but not in the root of *cpk21/23* and *nramp1* (Fig. 2 *D* and *E*). Again, loss of NRAMP1 function appeared to have a more detrimental effect (approximately 40% reduction) on shoot Mn accumulation than that of CPK21 and CPK23 (approximately 20% reduction). The physiological relevance of CPK21 and CPK23 was further reflected in a reduced efficiency of photosystem II in the double mutant under LMn supply, demonstrating the pivotal role of Mn in photosynthesis (*SI Appendix*, Fig. S4). Together, these findings identify the Ca^{2+}-regulated kinases CPK21 and CPK23 as crucially required for conferring LMn tolerance and suggest that these kinases exert their role via interaction with the NRAMP1 Mn-uptake transporter.

We next comparatively checked for the coexpression of *NRAMP1*, *CPK21*, and *CPK23* as a required prerequisite for a physiological meaningful interaction. Histochemical analysis of GUS activity of 7-d-old *ProNRAMP1:GUS*, *ProCPK21:GUS*, and *ProCPK23:GUS* transgenic plants showed that they all exhibited staining in roots (*SI Appendix*, Fig. S5*A*), which was consistent with previous reports (48, 49). In addition, *ProNRAMP1:NRAMP1-GFP*, *ProCPK21:CPK21-GFP*, and *ProCPK23:CPK23-GFP* transgenic lines were generated. We observed that these proteins were located at or in the plasma membrane of roots (*SI Appendix*, Fig. S5*B*). These results suggest that the tissue-specific expression patterns and subcellular localization of *NRAMP1*, *CPK21*, and *CPK23* were consistent with their common function.

Previously, it has been reported that *NRAMP1* expression responds to Mn deficiency (6). We next explored the expression patterns of *NRAMP1*, *CPK21*, and *CPK23* under Mn-depletion conditions. Upon transfer to Mn-deficient medium, the expression level of *NRAMP1* was up-regulated 2.5- to 3-fold within 12 h (*SI Appendix*, Fig. S5*C*). Moreover, expression of *CPK21* and *CPK23* was also transiently enhanced 1.5- to 2-fold within 12 h upon exposure to Mn deficiency, further correlating CPK21/23 function with Mn deficiency (*SI Appendix*, Fig. S5*C*).

Subsequently, we sought to further corroborate the CPK21/23–NRAMP1 interaction, which was initially identified by BiFC, through independent complementary experimental assays. To allow for split-luciferase complementation (LCI) assays in transiently transformed *N. benthamiana* leaves, *CPK21* and *CPK23* were fused to the N-terminal fragment of the *Photinus* luciferase (nLUC), and *NRAMP1* was fused to the C-terminal fragment of this luciferase (cLUC). Reconstitution of LUC activity indicative for protein–protein interaction was detected when either *CPK21-nLUC* or *CPK23-nLUC* were coexpressed with *NRAMP1-cLUC*. In contrast, coexpression of *CPK21/CPK23-nLUC* or *NRAMP1-cLUC* with the negative controls *GUS-cLUC* or *GUS-nLUC* did not restore LUC activity, supporting the specificity of the observed CPK21/23–NRAMP1 interaction (Fig. 3*A*).

To further validate these interactions in vitro, we performed glutathione S-transferase (GST) pull-down assays. Because we could not purify a full-length NRAMP1 fused with GST, we separately generated and purified GST fusion proteins that contained either the N-terminal cytoplasmic domain of NRAMP1 (NRAMP1-N; amino acid residues 1 to 44) or its C-terminal cytoplasmic domain (NRAMP1-C; amino acid residues 489 to 532). To obtain recombinant kinases, CPK21 was fused with a 6×His tag and an MBP tag, while CPK23 was combined with a 6×His epitope. Either CPK21 (with some traces of copurifying proteins) or CPK23 were separately coincubated with GST-NRAMP1-N, GST-NRAMP1-C, or GST, and pull-downs were performed with glutathione beads. After elution from the beads, immunoblot analyses were performed with anti-His antibodies to detect MBP-His-CPK21 and CPK23-His. Both, GST-NRAMP1-N and GST-NRAMP1-C were effective in pulling down MBP-His-CPK21, as well as CPK23-His (Fig. 3*B*). In contrast, GST alone did not retain either of the kinases. These results suggest that CPK21 and CPK23 both interact directly with the N terminus of NRAMP1 as well as with its C terminus.

To further investigate whether CPK21/23 interacted with NRAMP1 in vivo, we generated *ProCPK21:CPK21-3×FLAG* and *ProCPK23:CPK23-3×FLAG* transgenic lines in WT and *nramp1* mutant backgrounds. Proteins extracted from these transgenic plants were immunoprecipitated with anti-FLAG antibody-conjugated agarose and subjected to immunoblot analysis, and the precipitated NRAMP1 was detected with an

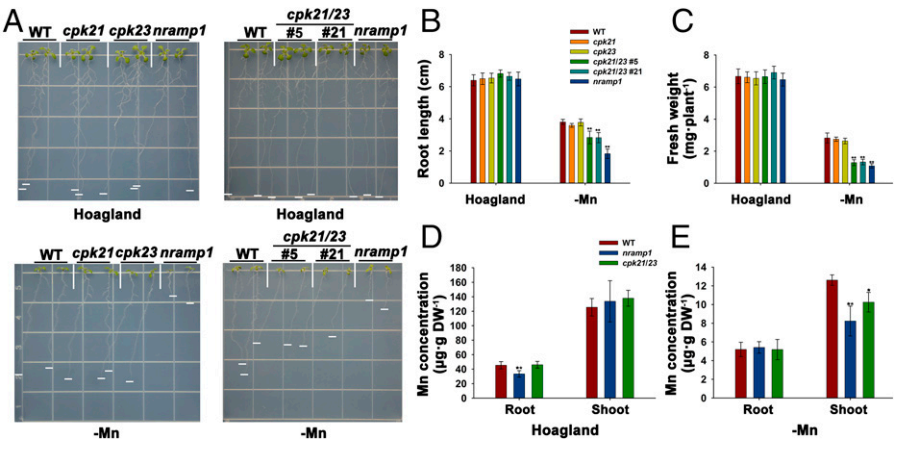

Fig. 2. Phenotypic analysis of *CPK21/23* single and double mutants. (*A*) Mn-deficiency phenotypes of mutants. The plants were grown on Mn-replete conditions and Mn-free conditions. (*B*) Statistical analysis of root lengths of plants shown in *A* (n = 16 seedlings; $^{**}P < 0.01$; Student's t test). (*C*) Statistical analysis of fresh weight of plants shown in *A* (n = 16 seedlings; $^{**}P < 0.01$; Student's t test). (*D*) Statistical analysis of Mn concentrations of plants under Hoagland medium shown in *A* (n = 3 biological replicates; $^{**}P < 0.01$; Student's t test). (*E*) Statistical analysis of Mn concentrations of plants under Mn deficiency shown in *A* (n = 3 biological replicates; $^{*}P < 0.05$, $^{**}P < 0.01$; Student's t test).

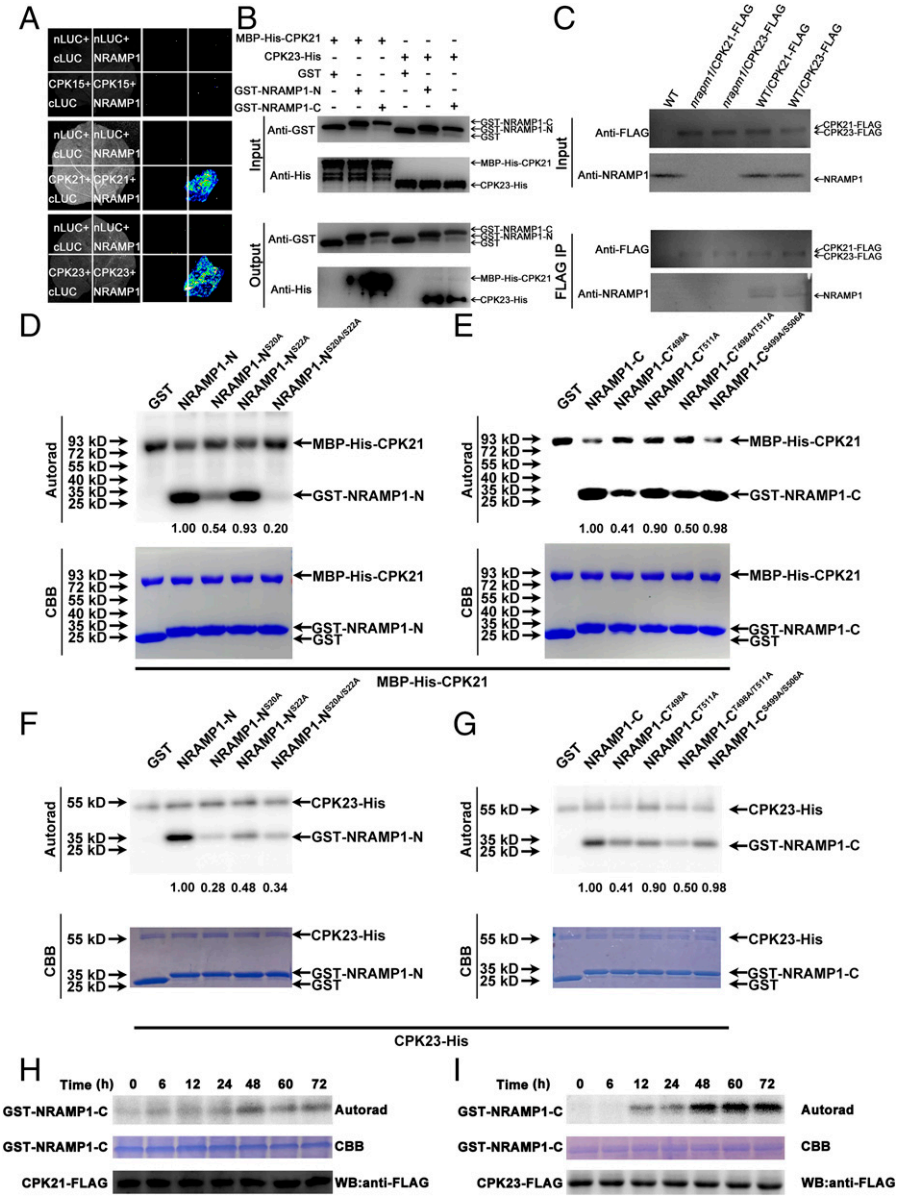

Fig. 3. CPK21 and CPK23 physically interacted with and phosphorylated NRAMP1. (*A*) LCI assay showing the interaction between CPK21/23 and NRAMP1. *N. benthamiana* leaves were coinfiltrated with *A. tumefaciens* cells containing different pairs of constructs. Luciferase images were captured using a cooled charge-coupled device imaging apparatus. (*B*) Pull-down assay showing the interaction of CPK21/23 and NRAMP1-N/C. CPK23 was fused to His, CPK21 to His-MBP, and NRAMP1-N/C to GST. Input and output were analyzed via Western blot with anti-His and anti-GST antibodies. (*C*) Coimmunoprecipitation of CPK21/23 with NRAMP1 in WT, *CPK21/23-FLAG/nramp1,* and *CPK21/23-FLAG/*WT transgenic plants. Proteins extracted were incubated with anti-FLAG antibody conjugated agarose. Input and immunoprecipitates were analyzed by immunoblotting using anti-FLAG and anti-NRAMP1 antibodies. (*D*) Identification of the phosphorylation target sites of CPK21 in NRAMP1-N. CPK21 was fused to His and MBP, whereas NRAMP1-N variants were fused to GST. The amount of protein loaded onto the gel was visualized by Coomassie brilliant blue (CBB), and phosphorylation was visualized by autoradiography (Autorad). (*E*) Identification of the phosphorylation target sites of CPK21 in NRAMP1-C. CPK21 was fused to His and MBP, whereas NRAMP1-C variants were fused to GST. (*F*) Identification of the phosphorylation target sites of CPK23 in NRAMP1-N. CPK23 was fused to His, whereas NRAMP1-N variants were fused to GST. (*G*) Identification of the phosphorylation target sites of CPK23 in NRAMP1-C. CPK23 was fused to His, whereas NRAMP1-C variants were fused to GST. (*H* and *I*) Protein kinase assay of CPK21 (*H*) or CPK23 (*I*) with NRAMP1-C under Mn deficiency. Ten-day-old seedlings were treated under Mn deficiency for indicated time periods. The protein kinases were quantified through Western blot and are shown at the bottom.

anti-NRAMP1 antibody. In WT/*ProCPK21:CPK21-3×FLAG* and WT/*ProCPK23:CPK23-3×FLAG* transgenic plants, NRAMP1 was efficiently immunoprecipitated with CPK21 or CPK23. While, NRAMP1 was not detected in immunoprecipitated samples of WT, *nramp1*/*ProCPK21:CPK21-3×FLAG*, and *nramp1*/*ProCPK23:CPK23-3×FLAG* transgenic plants (Fig. 3*C*). Altogether, these results establish that CPK21 and CPK23 directly interact with NRAMP1 in vitro and in vivo.

CPK Phosphorylation Targets S20/22 and T498 in NRAMP1. Phosphorylation of serine or threonine residues in substrate proteins is generally the consequence of CPK-target interaction (50, 51). To investigate whether CPK21 and CPK23 indeed directly phosphorylate NRAMP1, we first performed in vitro kinase assays that combined purified MBP-His-CPK21 or His-CPK23 kinase protein with either the NRAMP1 N-terminal domain (GST-NRAMP1-N) or the C-terminal domain of this transporter (GST-NRAMP1-C). Remarkably, both kinases efficiently phosphorylated the N as well as C termini of NRAMP1 in these assays, suggesting that both cytoplasmic domains of the transporter are subject to modification through phosphorylation by CPK21 and CPK23 (*SI Appendix*, Fig. S6*A*).

There are 12 Ser and 1 Thr residues in NRAMP1-N fragment, and 5 Ser and 3 Thr residues are found in NRAMP1-C fragment. To aid the identification of CPK target residues in NRAMP1-N and NRAMP1-C, we determined potential phosphorylation sites in both domains using the Group-based Prediction System web tool (gps.biocuckoo.cn/online.php). This approach identified Ser20, Ser22, Thr498, Ser499, Ser506, and Thr511 as potentially relevant CPK target residues (*SI Appendix*, Fig. S6*B*). We therefore generated several variants of NRAMP1 harboring nonphosphorylatable Ser(S)- or Thr(T)-to-Ala(A) point mutations, including NRAMP1-N^{S20A}, NRAMP1-N^{S22A}, NRAMP1-N$^{S20/22A}$, NRAMP1-C^{T498A}, NRAMP1-C^{T511A}, NRAMP1-C$^{S499/506A}$, and NRAMP1-C$^{T498/511A}$. Subsequently we exemplarily used CPK21 and CPK23 in vitro phosphorylation assays to assess the degree of phosphorylation of these substrates. These assays revealed that S22A substitution did not reduce the phosphorylation of the NRAMP1 N terminus, while the phosphorylation level of NRAMP1-N^{S20A} was substantially attenuated compared with NRAMP1-N. Notably, the phosphorylation of NRAMP1-N$^{S20/22A}$ appeared to be almost completely abolished, suggesting that phosphorylation of S20 may be required for efficient S22 phosphorylation (Fig. 3 *D* and *F*).

Phosphorylation analyses of the NRAMP1 C terminus revealed no difference in the phosphorylation level of NRAMP1-$C^{S499/506A}$ compared to NRAMP1-C (Fig. 3 *E* and *G*). In contrast, we detected a reduced but not fully abolished degree of phosphorylation of NRAMP1-C^{T498A} and NRAMP1-$C^{T498/511A}$ in these assays. These results identify S20 within the N terminus of NRAMP1 and T498 in its C terminus as primary target sites of CPK21 and CPK23 phosphorylation.

To elucidate whether phosphorylation may potentially exert a regulatory function on NRAMP1 in plants in response to Mn depletion, we assessed if the degree of NRAMP1 phosphorylation was affected by Mn deficiency. To this end, transgenic plants overexpressing *CPK21* or *CPK23* fused to FLAG tag were grown in Mn-deficient conditions for up to 72 h. CPK21 and CPK23 were extracted and enriched with anti-FLAG antibody-conjugated beads and then incubated with recombinant NRAMP1-C-GST purified from *Escherichia coli* in the presence of [γ-^{32}P] ATP (Fig. 3 *H* and *I*). We observed that phosphorylation of NRAMP1-C by CPK21 and CPK23 became enhanced from 6 h and 12 h of Mn deficiency, respectively, reaching a maximum after 48 h of Mn depletion. These findings suggest that Mn deficiency—most likely via the induction and continuation of long-lasting multicellular Ca^{2+} oscillation—induces and persistently further enhances the kinase activity of CPK21 and CPK23 toward NRAMP1 in plants.

NRAMP1^{T498} Phosphorylation Is Crucial for NRAMP1 Transport Activity. To elucidate the potential functional relevance of S20/22 and T498 phosphorylation, we conducted heterologous yeast complementation assays by expressing various nonphosphorylatable or phosphomimetic NRAMP1 variants in the yeast *Δsmf1*, a low-Mn–sensitive yeast mutant devoid of the major yeast high-affinity Mn uptake transporter Smf1 (52, 53). Semi–qRT-PCR assay confirmed a similar expression level of *NRAMP1* (*SI Appendix*, Fig. S6*A*). On media providing sufficient Mn supply, we did not observe any discernable growth differences among the various yeast strains. In contrast, upon supplementation of the media with 100 mM EGTA, which chelates divalent cations and thereby causes Mn depletion, obvious differences in the growth ability between different yeast strains became apparent. These stress conditions caused complete cessation of *Δsmf1* yeast containing only the empty vector, and dramatically reduced the growth ability of yeast expressing the nonphosphorylatable NRAMP1^{T498A} variant (Fig. 4*A*). In sharp contrast, *Δsmf1* yeast expressing NRAMP1, the nonphosphorylatable NRAMP1$^{S20/22A}$ variant, and the phosphomimetic NRAMP1$^{S20/22D}$ and NRAMP1^{T498D} variants all

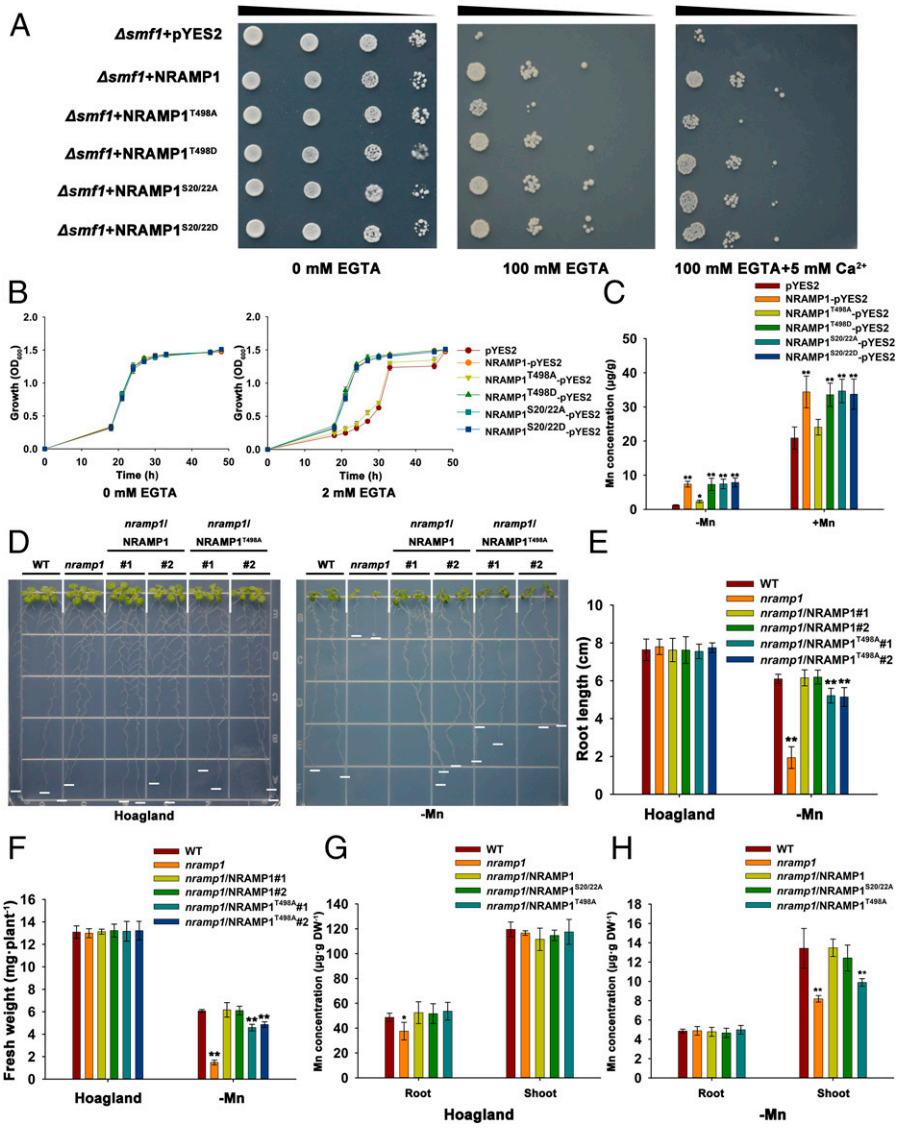

Fig. 4. Functional analysis of NRAMP1 phosphorylated by CPK21/23. (*A*) Empty vector (*Δsmf1*+pYES2), NRAMP1 (*Δsmf1*+NRAMP1), and NRAMP1 variants (*Δsmf1*+NRAMP1 variants) were transferred into the yeast mutant strain *Δsmf1*. Yeast cells were grown on medium SD-U (without uracil), SD-U added 100 mM EGTA (Mn^{2+} chelator), and SD-U added 100 mM EGTA and 5 mM $CaCl_2$. (*B*) Growth curves of yeast cells expressing pYES2, NRAMP1, and NRAMP1 variants were plotted from OD_{600} values. Growth of yeast cells in liquid cultures containing 0 or 2 mM EGTA was monitored every 3 h from 18 to 51 h (data are means ± SD $n = 3$ biological replicates). (*C*) ICP-MS analysis of Mn concentration in yeast cells carrying empty vector, NRAMP1, and NRAMP1 variants. The yeast cells grown on liquid medium SD-U and SD-U added 2 mM EGTA for 24 h. Data are means ± SD $n = 6$; $^*P < 0.05$, $^{**}P < 0.01$; Student's *t* test). (*D*) Mn-deficiency phenotypes of *ProNRAMP1:NRAMP1* and *ProNRAMP1:NRAMP1^{T498A}* transgenic plants. These plants were grown on Mn-replete conditions and Mn-free conditions. (*E*) Statistical analysis of root lengths of plants shown in *D* ($n = 16$ seedlings; $^{**}P < 0.01$; Student's *t* test). (*F*) Statistical analysis of fresh weight of plants shown in *D* ($n = 16$ seedlings; $^{**}P < 0.01$; Student's *t* test). (*G*) Statistical analysis of Mn concentrations of plants under Hoagland medium shown in *D* ($n = 3$ biological replicates; $^*P < 0.05$; Student's *t* test). (*H*) Statistical analysis of Mn concentrations of plants under Mn deficiency shown in *D* ($n = 3$ biological replicates; $^{**}P < 0.01$; Student's *t* test).

exhibited a similar degree of growth capability that was, however, substantially enhanced compared to the NRAMP1^{T498A} variant. In order to verify that the growth restriction of *Δsmf1* was caused by Mn deficiency rather than Ca^{2+} deficiency, we added 5 mM of $CaCl_2$ to the medium. In these conditions, yeast expressing the NRAMP1^{T498A} variant also exhibited reduced growth ability compared to yeast expressing NRAMP1 (Fig. 4*A*).

As a complementary assay providing alternative quantifiable values on the degree of mutant complementation, we performed growth-curve analysis of *Δsmf1* yeast expressing various plasmid combinations in media with or without addition of 2 mM EGTA. These assays revealed a strongly reduced growth rate of *Δsmf1* yeast containing either empty vector or the nonphosphorylatable NRAMP1^{T498A} variant specifically in Mn-deficient conditions, while all other NRAMP1 variants exhibited similar growth rates in Mn-replete or -deplete conditions (Fig. 4*B*). In addition, yeast expressing empty vector or NRAMP1^{T498A} accumulated less Mn than yeast expressing other NRAMP1 variants under both Mn sufficiency and Mn deficiency (Fig. 4*C*). These results establish phosphorylation of T498 as being critical for the Mn transport function of NRAMP1, while the phosphorylation status of S20/22 does not appear to modulate its transport activity.

Most recently, it has been reported that the phosphorylation status of S20/22/24 in NRAMP1 determines its plasma membrane retention in excess Mn conditions when overexpressed in *Arabidopsis* (42). We therefore investigated whether the phosphorylation status of T498 also affects the localization of NRAMP1. *NRAMP1-GFP* or *NRAMP1^{T498A}-GFP* fusions under control of the *CaMV 35S* promoter were transformed into *nramp1*. The resulting transgenic plants were grown on Hoagland medium and on Mn-deficiency medium for 7 d, and the fluorescence patterns were determined by confocal microscopy. The subcellular localization of NRAMP1-GFP and NRAMP1^{T498A}-GFP displayed no significant difference in roots, indicating that the phosphorylation of T498 does not influence the subcellular dynamics and localization of NRAMP1 (*SI Appendix*, Fig. S7*C*).

To address if the T498 phosphorylation status affects protein accumulation of NRAMP1, we performed Western blot analyses using a polyclonal antibody against NRAMP1 on total protein extracts isolated from WT and from plants expressing the nonphosphorylatable ProNRAMP1:NRAMP1^{T498A} grown on Hoagland medium. No difference in the accumulation of NRAMP1 or NRAMP1^{T498A} was detected, suggesting that the phosphorylation status of T498 does not affect the accumulation of NRAMP1 (*SI Appendix*, Fig. S7*D*).

In a complementary approach directly assessing a potential role of CPK21/23 and the impact of T498 phosphorylation on NRAMP1 protein stability, we extracted total protein from WT and *cpk21/23* grown for 7 d in Hoagland medium and subsequently exposed to Mn deficiency conditions for up to 72 h, either in the presence or the absence of 100 μM cycloheximide. We observed that the protein stability of NRAMP1 was unaffected under Mn-sufficient and -deficient growth conditions (*SI Appendix*, Fig. S7 *E–I*). In consequence, these results support the conclusion that CPK21/23-mediated NRAMP1 phosphorylation specifically regulates its transport function but does not appear to affect NRAMP1 abundance or localization upon sufficient or deficient Mn supply.

NRAMP1^{T498} Phosphorylation Facilitates NRAMP1-Mediated High-Affinity Mn Uptake in Plants. We next sought to resolve the physiological relevance of T498 phosphorylation. To this end, we generated plants expressing either *NRAMP1* or various *NRAMP1* variants under the control of the *NRAMP1* promoter in *nramp1*. First, we determined the expression level of NRAMP1 mRNA in WT and NRAMP1 variants transgenic lines by semi–qRT-PCR, and found that the expression level of NRAMP1 in WT and NRAMP1 variants transgenic lines was similar (*SI Appendix*, Fig. S7*B*). WT plants, *nramp1*, as well as plants expressing *ProNRAMP1:NRAMP1* or *ProNRAMP1:NRAMP1^{T498A}* were grown in Mn-sufficient and -deficient medium for 10 d (Fig. 4*C*). We noticed that expression of *NRAMP1* in *nramp1* fully restored the WT phenotype for all analyzed phenotypic parameters. Notably, plants expressing *NRAMP1^{T498A}* displayed only a partial rescue of the LMn-sensitive *nramp1* phenotype with regard to root length and fresh weight as phenotypic parameters (Fig. 4 *D* and *E*). These results reveal that phosphorylation of T498 is essential for conferring appropriate NRAMP1 function in Mn-deficiency tolerance.

For a complementary phenotyping assay WT, *nramp1*, *ProNRAMP1:NRAMP1*, *ProNRAMP1:NRAMP1$^{S20/22A}$*, and *ProNRAMP1:NRAMP1^{T498A}* plants were grown hydroponically in Hoagland medium for 2 wk and then transferred to Mn-deficiency medium for another 2 wk (*SI Appendix*, Fig. S8*A*). These assays again revealed that *ProNRAMP1:NRAMP1^{T498A}* plants displayed a sensitive phenotype in Mn-deficient conditions. Root length and fresh weight of these plants were similarly reduced as observed on solid media (*SI Appendix*, Fig. S8 *B* and *C*). In contrast, *ProNRAMP1:NRAMP1$^{S20/22A}$* plants exhibited no discernable differences in root length or fresh weight when compared to WT upon both sufficient and deficient Mn supply.

To ascertain the consequences of NRAMP1 transport activity regulation through T498 phosphorylation on plant Mn accumulation and homeostasis, we determined the Mn concentration in roots and shoots of WT, *nramp1*, *ProNRAMP1:NRAMP1*, and *ProNRAMP1:NRAMP1^{T498A}* plants grown on Hoagland or Mn-deficiency medium. The Mn concentration of *ProNRAMP1:NRAMP1^{T498A}* plants was decreased in shoots, while there was no significant difference in roots, similar to *nramp1* on Mn-deficient medium. On Hoagland medium, the Mn concentration of *nramp1* mutant in roots was decreased compared with WT. However, the Mn concentration in roots and shoots of *ProNRAMP1:NRAMP1$^{S20/22A}$* plants showed no obvious difference to that of the WT (Fig. 4 *F* and *G*). These results further reinforce Thr498 as crucial determinant of NRAMP1 Mn uptake activity. The defect in Mn uptake in *ProNRAMP1:NRAMP1^{T498A}* coincided with a decreased photosystem II quantum efficiency, confirming that phosphorylation at T498 impinges on photosynthetic efficiency, and hence plant productivity (*SI Appendix*, Fig. S4). Collectively, all of these ascertained consequences of distinct T498 phosphorylation statuses on plant growth and physiology further corroborate the conclusion that phosphorylation of T498, but not of S20/22 crucially determines the transport activity of NRAMP1.

NRAMP1^{T498} Phosphorylation Does Not Affect Fe Transport in Plants. NRAMP1 not only has Mn transport activity, but also displays Fe transport activity, thereby contributing to the loading of iron into seeds (54, 55). To elucidate the potential contribution of T498 phosphorylation to Fe transport activity of NRAMP1, we initially performed heterologous yeast complementation assays. We used the yeast mutant Δ*fet3fet4* (defective in Fe uptake at the plasma membrane) expressing NRAMP1 or NRAMP1 variants grown on SD/-Ura and SD/-Ura supplemented with 80 μM BPDS (chelating Fe ions) conditions to ascertain the effect of NRAMP1^{T498} phosphorylation on Fe transport activity. Remarkably, we did not observe any significant

difference in growth between yeast transformed with NRAMP1 or NRAMP1 variants (*SI Appendix*, Fig. S9*A*).

We then explored the potential impact of T498 phosphorylation on Fe transport in plants by analyzing transgenic plants expressing either NRAMP1 or the NRAMP1^{T498} variant. All the transgenic lines were grown in Fe-sufficient and -deficient medium for 10 d, respectively (*SI Appendix*, Fig. S8*B*). In these assays, lines expressing *ProNRAMP1:NRAMP1* or *ProNRAMP1:NRAMP1*^{T498A} displayed no discernable difference in root length and fresh weight compared with WT (*SI Appendix*, Fig. S9 *C* and *D*). These results indicate that the NRAMP1^{T498} phosphorylation does not affect Fe uptake into plants.

CPK Activity Constitutes a Rate-Limiting Step in the Ca^{2+}-CPK21/23-NRAMP1 Axis for Facilitating Mn Uptake. To further assess the specific role of CPK21 and CPK23 in the tolerance to Mn deficiency, we devised a complementary genetic approach by individually overexpressing (OE) either of both kinases constitutively. To this end, we generated *Arabidopsis* plants overexpressing either *CPK21* or *CPK23* by introducing the coding sequence of *CPK21*/*23* into the pCAMBIA1307-FLAG vector under control of the *CaMV 35S* promoter. Enhanced expression of the kinases in *CPK21*-OE or *CPK23*-OE plants was verified via qRT-PCR (*SI Appendix*, Fig. S10). Plants overexpressing *CPK23* displayed enhanced root growth and higher fresh weight specifically under Mn-deficient conditions when compared to WT (Fig. 5 *A*–*C*). These results support the notion that an increased expression of *CPK23* is sufficient to enhance NRAMP1 Mn uptake activity and to confer enhanced tolerance to Mn depletion via the CPK23-NRAMP1 axis. In contrast to the overexpression of *CPK23*, overexpression of *CPK21* did not cause any discernable differences to WT plants in normal and Mn-deficient conditions (Fig. 5 *A*–*C*). In conclusion, elevated expression of *CPK21* is not sufficient to enhance LMn tolerance.

These observations align with the fact that the two closely related kinases, CPK21 and CPK23, share their substrate specificity but exhibit remarkable differences in their Ca^{2+} affinity and in the dependence of their kinase activity on the cellular Ca^{2+} concentration (49, 56–60). CPK23 is already largely active at basal Ca^{2+} concentrations, and further elevations of Ca^{2+} do not significantly enhance kinase activity. Therefore, increasing the amounts of CPK23 protein is sufficient to enhance NRAMP1 Mn uptake activity and to confer enhanced tolerance to Mn depletion via the Ca^{2+}-CPK23-NRAMP1 axis. CPK21 displays a fundamentally different Ca^{2+} dependence. This kinase remains inactive at resting Ca^{2+} concentrations (below 200 nM) and

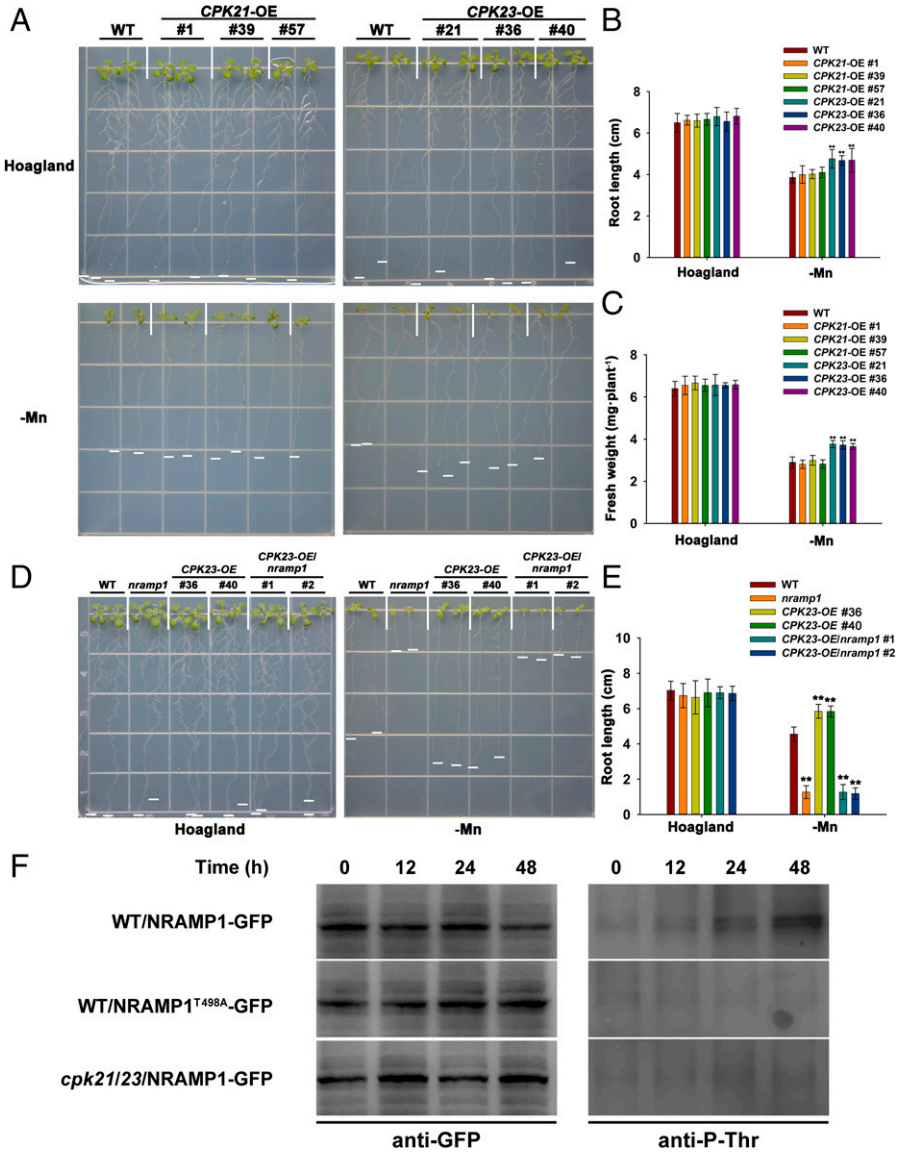

Fig. 5. Genetic interaction of CPK21/23 with NRAMP1. (*A*) Mn-deficiency phenotypes of *CPK21/23* overexpression plants. The plants were grown on Mn-replete conditions and Mn-free conditions. (*B*) Statistical analysis of root lengths of plants shown in *A* (n = 16 seedlings; $^{**}P < 0.01$; Student's t test). (*C*) Statistical analysis of fresh weight of plants shown in *A* (n = 16 seedlings; $^{**}P < 0.01$; Student's t test). (*D*) Mn-deficiency phenotype of *CPK23*-OE/*nramp1*. (*E*) Statistical analysis of primary root lengths of plants shown in *D* (n = 16 seedlings; $^{**}P < 0.01$; Student's t test). (*F*) The seedlings were treated with Mn-deficient conditions for 0, 12, 24, and 48 h, respectively. The signal of NRAMP1 and GFP were detected by P-Thr antibody and GFP antibody, respectively.

becomes only activated upon elevated Ca^{2+} concentrations as they result from Ca^{2+} signals. In conclusion, elevated expression of CPK21 protein alone without corresponding amplification of Ca^{2+} signals are not sufficient to enhance LMn tolerance. Therefore, this finding also suggests that the amplitude and general intensity of the LMn-induced Ca^{2+} signals represent a rate-limiting factor in conveying LMn adaptation via the Ca^{2+}-CPK21-NRAMP1 axis.

We also assessed the genetic interaction of CPK21 and CPK23 with NRAMP1. *CPK23* was overexpressed in *nramp1* by crossing *CPK23*-OE and *nramp1* plants. We then scored the growth phenotypes of *CPK23*-OE/*nramp1* plants in comparison to WT and *nramp1* (Fig. 5*D*). Specifically, under Mn deficiency, root growth of *CPK23*-OE/*nramp1* plants was significantly decreased to an extent comparable to *nramp1* plants (Fig. 5*E*). Collectively, these results reinforce that CPK21/23 exerts its regulating function in establishing Mn-deficiency tolerance by activating the high-affinity Mn uptake transporter NRAMP1 and thereby further corroborate the existence and physiological relevance of the LMn-Ca^{2+}-CPK21/23-NRAMP1 signaling axis.

To further mechanistically interconnect these phenotypes with the CPK activation-dependent phosphorylation status of Thr498, we performed a time series phosphorylation analysis of NRAMP1 in response to Mn deprivation. To this end, transgenic plants overexpressing C-terminally GFP-tagged *NRAMP1*/*NRAMP1*^{T498A} in WT or *cpk21*/*23* mutant were exposed to Mn deficiency for 0, 12, 24, and 48 h, respectively. From these plants, NRAMP1 was extracted and enriched with GFP beads, and the phosphorylation level of NRAMP1 was detected using a P-Thr antibody. In general, the phosphorylation level of NRAMP1 was notably decreased in *cpk21*/*23*/NRAMP1-GFP or WT/NRAMP1^{T498A}-GFP transgenic plants compared with the WT/NRAMP1-GFP plants. In addition, we observed that phosphorylation of NRAMP1 was also significantly enhanced after 6 h of Mn deficiency, reaching a maximum after 48 h of Mn depletion in WT/NRAMP1-GFP. The timing and intensity of NRAMP1 phosphorylation modulation was consistent with the observed CPK21/23 activation also starting at 6 h and reaching a maximum after 48 h of LMn treatment. In contrast, the NRAMP1 phosphorylation level in *cpk21*/*23*/NRAMP1-GFP or WT/NRAMP1^{T498A}-GFP transgenic plants was practically unaltered (Fig. 5*F*). Taken together, these results clearly establish that the Mn deficiency-induced phosphorylation of Thr498 in NRAMP1 is strictly dependent on CPK21/23 activity. Moreover, these data identify LMn/Ca^{2+} signal-triggered CPK activation as causative for enhanced and sustained NRAMP1 phosphorylation.

Discussion

A Multicellular Functionally Defined LMnSN Creates a Complex Oscillatory Ca^{2+} Pattern as a Primary Response to Mn Deficiency. The creation of ultrasensitive Ca^{2+} reporter proteins paved the way for capturing the occurrence of Ca^{2+} signals in biological processes, for which formerly the limiting sensitivity of existing Ca^{2+} reporters prevented to detect the potential involvement of this phenomenon. Here, we employed the GCaMP6f-mCherry Ca^{2+} reporter that favorably combines the superior dynamic range and temporal accuracy of GCaMP6f with ratiometric data acquisition provided by normalization through mCherry emission monitoring. This enabled us to discover the occurrence of specific Ca^{2+} signals in *Arabidopsis* roots as signaling response to insufficient Mn supply.

In these analyses, we did not discern LMn-specific fast Ca^{2+} signals occurring within the first minutes of Mn depletion, but further validated and refined recently described fast-occurring (within 15 min) Ca^{2+} signals upon exposure to HMn. These signals occurred in a HMnSN encompassing the outer cell layers of the MZ/EZ border region of roots as specific response to HMn exposure. In contrast, LMn-specific Ca^{2+} signals initiated beginning from 120 min after cessation of Mn supply and lasted throughout the measurement period of 6 h. Although the whole root was evenly challenged with decreasing Mn availability, these LMn-specific Ca^{2+} signals were confined around the central EZ, suggesting a functional relevance of this spatially highly defined signal pattern. Notably, the spatial pattern of these LMn-specific Ca^{2+} signals precisely coincide with the previously defined expression pattern of the NRAMP1 Mn uptake transporter that is caused by extended exposure to limited Mn supply, potentially linking these Ca^{2+} signals to NRAMP1 function (6). Addressing whether the exceptional response capability of these cells results from more pronounced Mn concentration decline in this region, from enhanced Mn-sensing sensitivity, or from a specific equipment with Mn-sensing/signaling components provides a significant direction for future research.

Strikingly, the LMn-induced Ca^{2+} signals described here displayed an astonishing oscillatory nature that has so far not been observed in response to any abiotic environmental cue triggering Ca^{2+} signal formation in plants. These multicellular Ca^{2+} oscillations began 120 min after onset of LMn supply, exhibited an individual duration of 30 min, and displayed an invariant amplitude throughout their occurrence. The silent lack time of 120 min before signaling initiation suggests that an intracellular, perhaps cytoplasmic decline of Mn concentration represents the required trigger and that the sensing of Mn status takes place intracellularly, as recently described for the regulation of the metal uptake transporter IRT1 (41).

An important deduction emanating from our observations is the functional definition of an LMnSN as multicellularly organized center of LMn-induced Ca^{2+} signal formation. This LMnSN is located proximal to the low-K^+-sensing niche (KSN) that we most recently identified and characterized as the center of primary Ca^{2+} signal formation of plants encountering K^+ depletion in their rhizosphere (61). However, LMnSN and KSN obviously share their multicellular character, which apparently is defined by functional properties of these cells that do not correlate with morphologically recognizable features of their differentiation. By using high-resolution Ca^{2+} dynamics analyses, we revealed a cell layer-wise successive Ca^{2+} concentration alteration progressing root-inward from the epidermis to the stele during Ca^{2+} oscillation build-up, while proceeding in the opposite direction during oscillation decline. Moreover, we also uncovered longitudinal Ca^{2+} signal expansion as an inherent feature of each individual oscillation created by the LMnSN. Remarkably, the longitudinal Ca^{2+} signal spreading was initiated only after the absolute maximum of Ca^{2+} concentration increase in the stelar cell files was reached. Collectively, these findings identify and define a multicellular Ca^{2+} signaling center that, although it logically has to represent a functional unit in terms of response implementation, exhibits a remarkably diverse, but obviously mutually interdependent diversity of cytoplasmic Ca^{2+} signatures in individual cells that form its cellular building blocks. Consequently, formation of such spatiotemporally defined signal oscillations within complex tissues, which are built through highly coordinated interdependent Ca^{2+} fluctuations in individual cells, demands highly sophisticated cell-to-cell tuning mechanisms for implementation.

A Ca^{2+}-CPK21/23-NRAMP1 Axis Augments Plant Mn Uptake upon Mn Deficiency. In order to decipher how these recently discovered Ca^{2+} signals translate into cellular and organismic adaptation of *Arabidopsis* to LMn, we focused on the key Mn uptake transporter NRAMP1 and elucidated the potential involvement of CPKs, a family of protein kinases known to convey Ca^{2+}-dependent target phosphorylation, in NRAMP1 regulation. This approach identified CPK21 and CPK23 as interacting with NRAMP1 and as phosphorylating this Mn transporter at S20 and T498.

Recently, is has been reported that in conditions of toxic HMn supply, the phosphorylation status of S20 exerts a crucial role in conferring tolerance to these conditions, in that phosphorylation of this residue enhances NRAMP1 endocytotic internalization to reduce Mn uptake (42). Here, our investigations did not reveal a discernable role of S20 under conditions of insufficient Mn supply, as we did not detect an impact of the S20 phosphorylation status on the uptake capability of NRAMP1 in yeast mutant complementation assays and found that plants expressing the nonphosphorylatable $NRAMP1^{S20/22A}$ variant in *nramp1* did not exhibit significant phenotypic differences compared with WT and plants expressing WT *NRAMP1* in Mn-sufficient and Mn-deficient conditions. However, our investigations identified the phosphorylation status of T498 as a crucial determinant of NRAMP1 Mn uptake capability. Accordingly, the $NRAMP1^{T498A}$ variant was less effective in restoring the Mn uptake activity of the respective yeast mutants than WT *NRAMP1* and, moreover, plants expressing the nonphosphorylatable variant $NRAMP1^{T498A}$ in *nramp1* displayed only partial complementation of the investigated LMn-sensitive phenotypes. Nevertheless, expression of $NRAMP1^{T498A}$ in *nramp1* conferred a partial restauration of LMn tolerance. This observation suggests either an inherent basal transport activity of NRAMP1 independent of its phosphorylation status, or the existence of alternative mechanisms as contributing to NRAMP1 regulation.

Our reverse genetics analyses of CPK21 and CPK23 function did not indicate discernable physiological or developmental alterations in individual mutants of both kinases. However, *cpk21/23* double mutants exhibited a significant impairment of their LMn tolerance that manifested through reduced root growth, lower fresh weight, and diminished Mn accumulation compared to WT. These phenotypic alterations from WT were not as severe as that of *nramp1* mutants, suggesting that either additional regulatory components/mechanisms impact on NRAMP1 uptake activity or that—alternatively but not mutually exclusive—NRAMP1 displays constitutive basal activity independent of its phosphorylation status. The comprehensive impairment in LMn tolerance of *cpk21/23* mutants establishes a critical role of appropriate NRAMP1 regulation through the activity of both kinases and defines a Ca^{2+}-CPK21/23-NRAMP1 axis for conferring plant adaptation to Mn depletion. Notably, the timing of events that we discovered at different mechanistic levels, including the onset of Ca^{2+} oscillations beginning from 2 h of Mn depletion, enhanced CPK activity clearly detectable from 6 h, and pronounced increasing NRAMP1 phosphorylation starting from 6 h, supports a causative chain for enhanced Mn uptake that is built through successive Ca^{2+} signal formation, CPK activation, and NRAMP1 activity up-regulation.

An Emerging Ca^{2+} Network Controlling and Coordinating Plant Mn Homeostasis. We recently identified a vacuolar Ca^{2+}-kinase transporter module as being most relevant for plant adaptation to HMn exposure and for fine-tuning Mn homeostasis (37, 38). In contrast to the Ca^{2+} oscillation discovered here in response to Mn depletion, excess Mn triggers a rapid monoamplitude Ca^{2+} signal spatially separated from the LMnSN. As a downstream response, the four Ca^{2+}-dependent kinases CPK4/5/6/11 activate vacuolar Mn uptake through phosphorylation of the tonoplast-localized Mn transporter MTP8 primarily at S31/32 to sequester excess Mn into the vacuole. This process confers plant protection from Mn toxicity (34). This vacuolar sequestration mechanism is subsequently counteracted through another Ca^{2+}-activated phosphorylation module for optimally balancing plant growth and Mn homeostasis. This is brought about by phosphorylation of MTP8 at an alternative residue (S35) through the action of the Ca^{2+} sensors CBL2 and CBL3 that recruit CIPK3/9/26 to inhibit MTP8 transport activity. Such a "gas and brake" mechanism thereby provides a means for precise regulation of vacuolar Mn sequestration in plants (35).

Collectively, our findings reported here and the well-established differential Ca^{2+} dependence of both kinases suggest a switch-like mechanism of Ca^{2+} signaling via CPK21 and CPK23 in conferring plant tolerance to Mn deficiency. Under sufficient Mn supply and mild Mn depletion, CPK23 would confer a basal phosphorylation level of NRAMP1 that is sufficient to meet the demand of the plant. Ca^{2+} oscillations in the root EZ, as they are triggered by severe decline in Mn availability, would result in additional activation of CPK21 that further facilitates NRAMP1 phosphorylation and thereby increases the share of phosphorylated and hence activated NRAMP1 proteins, which are also becoming more abundant as a consequence of transcriptional *NRAMP1* induction upon Mn depletion. Consequently, this Ca^{2+} switch mechanism, constituted by the Ca^{2+}-CPK23-NRAMP1 and the Ca^{2+}-CPK21-NRAMP1 axes, allows for appropriately fine-tuning plant Mn uptake and homeostasis under conditions of insufficient Mn supply (Fig. 6). The emergent versatility of Ca^{2+} control in Mn transport will allow for further dissecting, if the involvement of Ca^{2+}-dependent phosphorylation potentially provides a means for aligning Mn fluxes across the different membrane compartments in plants.

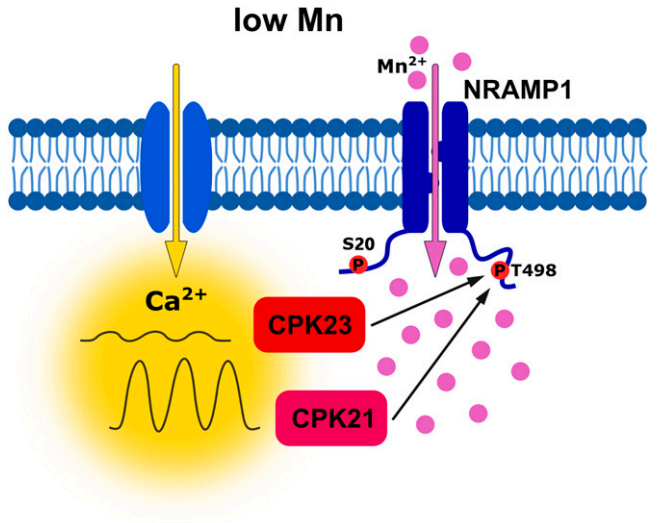

Fig. 6. Model for LMn signaling and NRAMP Mn uptake regulation in *Arabidopsis*. Plant exposure to insufficient Mn supply triggers long-lasting oscillatory Ca^{2+} signals. Already under replete Mn supply and mild Mn depletion, CPK23 confers basal phosphorylation of NRAMP1 at T498. Through Ca^{2+} oscillations triggered by severe decline in Mn availability, additional activation of NRAMP1 through CPK21-mediated phosphorylation at T498 further facilitates enhanced Mn uptake. This Ca^{2+} switch mechanism, constituted by the Ca^{2+}-CPK23-NRAMP1 and the Ca^{2+}-CPK21-NRAMP1 axes, allows for appropriately fine-tuning plant Mn uptake and homeostasis under conditions of insufficient Mn supply.

Materials and Methods

Plant Materials and Growth Conditions. Columbia (Col-0) was used as control for all experiments. The T-DNA insertion lines were *cpk21* (SALK_043765), *cpk23* (SALK_007958), and *nramp1* (SALK_053236C). *Arabidopsis* seeds were surface-sterilized and then stratified for 3 d at 4 °C. The seeds were grown on a nutrient medium consisting of 1.2% agar (Sigma-Aldrich, A1296), 2% sucrose, and full-strength Hoagland nutrient solution [5 mM KNO_3, 5 mM $Ca(NO_3)_2$, 2 mM $MgSO_4$, 1 mM $NH_4H_2PO_4$, 20 μM $MnSO_4$, 3 μM H_3BO_3, 1 μM $(NH_4)_6Mo_7O_{24}$, 0.4 μM $ZnSO_4$, 0.2 μM $CuSO_4$, 20 μM Fe (III)-EDTA] at pH 5.75∼5.85 (33). To conduct Mn-deficiency treatments, the Hoagland medium was supplemented without $MnSO_4$. The Fe-deficiency medium, consisting of 1% agar (Sigma-Aldrich, A1296), 1% sucrose, and full-strength Hoagland nutrient solution without Fe (III)-EDTA, was additionally supplemented with 10 μM Ferrozine. To grow plants in the soil, 7-d-old seedlings grown on Hoagland medium were transferred to nutrient-rich soil (Pindstrup substrate, Denmark) and grown in a greenhouse under controlled conditions (22 °C/19 °C, 16-h light/8-h dark, regime with light intensity adjusted to 120 μmol m^{-2} s^{-1}).

Ratiometric Ca^{2+} Imaging. Ratiometric Ca^{2+} imaging was performed as described previously (45, 62). Plants expressing the ratiometric Ca^{2+} indicator GCaMP6f-mCherry were grown on Hoagland media for 4 to 5 d and imaged in Hoagland buffer containing 20 μM $MnSO_4$, or 1.5 mM $MnSO_4$ (HMn), or 0 μM $MnSO_4$ and 2.5 μM EGTA (0 Mn, LMn), respectively. Seedlings were mounted in custom flowthrough chambers. For short-term imaging (30 min), the acquisition interval was set to 6 s; for long-term measurements (6 h), the interval was set to 2 min. For epifluorescence measurements using a Zeiss Axio observer imaging station, GFP signal was detected with Ex470/40 and Em525/50 filters; mCherry signal was detected with Ex560/40 and Em630/75 filters. High-resolution microscopy was performed at a Leica SP8 confocal laser-scanning microscope. GFP was excited with an Argon laser (488 nm) and emission signal was collected at 500 to 540 nm; mCherry was excited with a white light laser at 561 nm and emission signal was collected at 580 to 640 nm.

For the representation of Ca^{2+} dynamics, the GFP signal was normalized to the mCherry signal, and the ratio was depicted in false color using ImageJ. For Ca^{2+} dynamics quantification the ratio values were normalized to the baseline (R_0) to obtain relative ratio changes for all measured timepoints ($\Delta R/R_0$) as described previously for the Ca^{2+} sensor YC3.6 (63). Data analysis of high-resolution confocal laser-scanning microscopy images was performed, as describes previously (64).

Phenotypic Analysis of Seed Germination. For phenotypic analysis of germination, surface-sterilized seeds were transferred to Hoagland medium or Mn-deficiency medium described above for 10 d. The root length was measured with ImageJ.

Elemental Analysis. To verify the effects of Mn uptake on plant growth, seedlings of WT, *nramp1 ProNRAMP1:NRAMP1*, and *ProNRAMP1:NRAMP1* transgenic plants cultured 2 wk on hydroponics were transferred to Mn deficiency for another 2 wk. The samples were analyzed by inductively coupled plasma–mass spectrometry (ICP-MS).

CRISPR/Cas9. Primers were designed online (crispor.tefor.net/crispor.py) and connect sgRNA to pHEE401 vector. The sequence of sgRNA target to *CPK21* is GTTCAAACCCATGTAGTCCC. The homozygous *cpk21/23* double mutants (*cpk21/23* #5 and *cpk21/23* #21) are a frameshift mutation that *cpk21/23* #5 added a base and *cpk21/23* #21 deleted eight bases in the first exon of *CPK21*.

BiFC Assay. BiFC assay was conducted as previously published (65, 66). In brief, resuspension buffer (10 mM $MgCl_2$; 10 mM MES, pH = 5.6) was used to adjust the final concentration of the strain to a specific OD at 600 nm (OD_{600}). The fluorescence signals were detected using a confocal laser-scanning microscope (Olympus IX83-FV3000).

LCI Assay. LCI was conducted according to a previously published method (67). The OD_{600} values of CPK21/23-nLUC and NRAMP1-cLUC were adjusted to 1.5, and that of P19 was adjusted to 1.0. The signals were detected by CCD (Princeton, Lumazone Pylon 2048B).

Coimmunoprecipitation. Coimmunoprecipitation assay was conducted according to a previously published method (67). CPK21/23 and NRAMP1 were detected with anti-FLAG antibody (TransGen Biotech) and anti-NRAMP1 antibody (TransGen Biotech), respectively.

In Vitro and In Vivo Phosphorylation Analysis. The in vitro kinase assay was conducted according to a previously published method (37). For the in vivo kinase assay, constructs of *NRAMP1-GFP*, *NRAMP1^{T498A}-GFP* were transformed into WT or *cpk21/23* mediated by *Agrobacterium tumefaciens*. The GFP signals were detected with anti-GFP antibody (TransGen Biotech), and the phosphorylation signals were analyzed by Western blotting using a phospho-threonine antibody (Cell Signaling Technology).

GST Pull-Down Assay. GST pull-down assay followed a previously published method (37). In brief, 5 mg of purified GST or GST-NRAMP1-N/C fusion protein was incubated with glutathione beads (GE Healthcare) at 4 °C for 2 h, then incubated with 1 mg of MBP-His-CPK21 or CPK23-His for another 2 h, and then the beads washed six times with PBS buffer (pH = 7.4). After elution from the beads, the proteins were subjected to immunoblot analysis with anti-His antibody (TransGen Biotech) to detect His-CPK21/23.

Subcellular Localization of NRAMP1. The NRAMP1-GFP transgenic plants were grown vertically under Mn-supplied and Mn-deficiency conditions. GFP fluorescence was observed using a confocal microscope (FV3000). The excitation wavelength was 488 nm, and emission wavelength was between 500 and 530 nm.

Functional Analysis in Yeast. *NRAMP1* was cloned into the yeast expression vector pYES2 and transformed into the yeast strain *Δsmf1* and *Δfet3fet4*. The transgenic yeast strain was grown in SD/-Ura medium for 5 to 7 d. SD/-Ura liquid medium was used to culture yeast to OD_{600} = 0.1. Under sterile conditions, four 10-fold gradient dilutions were established, and 2 μL of each gradient dilution was spotted onto the medium with 100 mM EGTA and 80 μM BPDS, respectively.

The yeast cells with different vectors were grown on liquid medium SD-U and SD-U added 2 mM EGTA for 24 h. The yeast cells were harvested by centrifugation at 700 × *g* for 5 min and three times with 10 mM disodium EDTA, before being washed once in water. The samples were dried and digested follow the above method.

Photosynthesis Measurements. To determine maximum quantum efficiency of photosystem II photochemistry (Fv/Fm), sterile and stratified seeds were sown on 1/2 Murashige & Skoog plates containing 8 g L^{-1} agar (pH 5.8). After 14 d, seedlings were transferred to liquid culture medium. Plants were cultivated on full nutrient solution for another 14 d and then transferred to either control or Mn-free conditions for 10 d. Photosynthetic parameters were determined by PAM fluorescence imaging (IMAGING-PAM M-Series, Walz). Before measurements, plants were dark-adapted for 30 min. Images were captured, and saturating flashes (902 μmol m^{-2} s^{-1}) were used to measure Fv/Fm.

Data, Materials, and Software Availability. All study data are included in the main text and supporting information.

ACKNOWLEDGMENTS. We thank Dr Weihua Wu (State Key Laboratory of Plant Physiology and Biochemistry, China Agricultural University, Beijing, China) for *ProCPK21:GUS* and *ProCPK23:GUS* transgenic lines; Dr. Chaofeng Huang (National Key Laboratory of Plant Molecular Genetics, Shanghai Center for Plant Stress Biology) for yeast strain *Δsmf1*, the *ProNRAMP1:GUS* transgenic line, and *nramp1* mutant seeds; Dr. Qijun Chen (State Key Laboratory of Plant Physiology and Biochemistry, China Agricultural University, Beijing, China) for CRISPR/Cas9 toolkit pHEE401 and pCBC-dT1T2; Dr. Rainer Waadt (Westfälische Wilhelms Universität Münster) for providing GCaMP6f-mCherry sensor lines; and Dr. Xueling Huang, Dr. Hua Zhao, and Dr. Fengping Yuan (State Key Laboratory of Crop Stress Biology for Arid Areas, Northwest A&F University, Yangling, China) for technique assistance. This research was funded by National Natural Science Foundation of China Grants 32222008 (to C.W.), 32100215 (to P.H.), and 31900236 (to Z.Z.); and partly supported by the open funds of China Postdoctoral Science Foundation 2018M643740 (to Z.Z.) and the Natural Science Basic Research Plan in Shaanxi Province of China (Program 2019JQ-150). J.K. gratefully acknowledges support through a grant provided by the Deutsche Forschungsgemeinschaft (INST211/853-1 FUGG).

Author affiliations: [a]State Key Laboratory of Crop Stress Biology for Arid Areas, College of Life Sciences, Northwest A&F University, 712100 Shaanxi, China; [b]Biotechnology Research Institute, Chinese Academy of Agricultural Sciences, 100081 Beijing, China; [c]Institut für Biologie und Biotechnologie der Pflanzen, Westfälische Wilhelms Universität, 48149 Münster, Germany; and [d]Plant Nutrition Laboratory, Institute of Agricultural and Nutritional Sciences, Martin Luther University Halle-Wittenberg, 06108 Halle, Germany

1. K. J. Horning, S. W. Caito, K. G. Tipps, A. B. Bowman, M. Aschner, Manganese is essential for neuronal health. *Annu. Rev. Nutr.* **35**, 71–108 (2015).
2. L. Li, X. Yang, The essential element manganese, oxidative stress, and metabolic diseases: Links and interactions. *Oxid. Med. Cell. Longev.* **2018**, 7580707 (2018).
3. S. Alejandro, S. Höller, B. Meier, E. Peiter, Manganese in plants: From acquisition to subcellular allocation. *Front Plant Sci* **11**, 300 (2020).
4. E. Andresen, E. Peiter, H. Küpper, Trace metal metabolism in plants. *J. Exp. Bot.* **69**, 909–954 (2018).
5. S. B. Schmidt, P. E. Jensen, S. Husted, Manganese deficiency in plants: The impact on photosystem II. *Trends Plant Sci.* **21**, 622–632 (2016).
6. R. Cailliatte, A. Schikora, J. F. Briat, S. Mari, C. Curie, High-affinity manganese uptake by the metal transporter NRAMP1 is essential for Arabidopsis growth in low manganese conditions. *Plant Cell* **22**, 904–917 (2010).
7. L. Castaings, A. Caquot, S. Loubet, C. Curie, The high-affinity metal transporters NRAMP1 and IRT1 team up to take up iron under sufficient metal provision. *Sci. Rep.* **6**, 37222 (2016).
8. S. Alejandro *et al.*, Intracellular distribution of manganese by the *Trans*-Golgi network transporter NRAMP2 is critical for photosynthesis and cellular redox homeostasis. *Plant Cell* **29**, 3068–3084 (2017).
9. E. L. Bastow *et al.*, Vacuolar iron stores gated by NRAMP3 and NRAMP4 are the primary source of iron in germinating seeds. *Plant Physiol.* **177**, 1267–1276 (2018).
10. A. Sasaki, N. Yamaji, K. Yokosho, J. F. Ma, Nramp5 is a major transporter responsible for manganese and cadmium uptake in rice. *Plant Cell* **24**, 2155–2167 (2012).
11. L. Li *et al.*, NRAMP6 and NRAMP1 cooperatively regulate root growth and manganese translocation under manganese deficiency in Arabidopsis. *Plant J.* **110**, 1564–1577 (2022).
12. N. H. Cheng, J. K. Pittman, T. Shigaki, K. D. Hirschi, Characterization of CAX4, an Arabidopsis $H(^{+})$/cation antiporter. *Plant Physiol.* **128**, 1245–1254 (2002).
13. K. D. Hirschi, V. D. Korenkov, N. L. Wilganowski, G. J. Wagner, Expression of Arabidopsis CAX2 in tobacco. Altered metal accumulation and increased manganese tolerance. *Plant Physiol.* **124**, 125–133 (2000).
14. H. Mei *et al.*, Root development under metal stress in *Arabidopsis thaliana* requires the H^{+}/cation antiporter CAX4. *New Phytol.* **183**, 95–105 (2009).
15. S. A. Kim *et al.*, Localization of iron in Arabidopsis seed requires the vacuolar membrane transporter VIT1. *Science* **314**, 1295–1298 (2006).
16. Y. Zhang, Y. H. Xu, H. Y. Yi, J. M. Gong, Vacuolar membrane transporters OsVIT1 and OsVIT2 modulate iron translocation between flag leaves and seeds in rice. *Plant J.* **72**, 400–410 (2012).
17. G. Vert *et al.*, IRT1, an Arabidopsis transporter essential for iron uptake from the soil and for plant growth. *Plant Cell* **14**, 1223–1233 (2002).
18. M. J. Milner, J. Seamon, E. Craft, L. V. Kochian, Transport properties of members of the ZIP family in plants and their role in Zn and Mn homeostasis. *J. Exp. Bot.* **64**, 369–381 (2013).
19. S. Eroglu, B. Meier, N. von Wirén, E. Peiter, The vacuolar manganese transporter MTP8 determines tolerance to iron deficiency-induced chlorosis in Arabidopsis. *Plant Physiol.* **170**, 1030–1045 (2016).
20. S. Eroglu *et al.*, Metal tolerance protein 8 mediates manganese homeostasis and iron reallocation during seed development and germination. *Plant Physiol.* **174**, 1633–1647 (2017).
21. E. Delhaize *et al.*, A role for the AtMTP11 gene of Arabidopsis in manganese transport and tolerance. *Plant J.* **51**, 198–210 (2007).
22. E. Peiter *et al.*, A secretory pathway-localized cation diffusion facilitator confers plant manganese tolerance. *Proc. Natl. Acad. Sci. U.S.A.* **104**, 8532–8537 (2007).
23. Z. Wu *et al.*, An endoplasmic reticulum-bound $Ca(^{2+})/Mn(^{2+})$ pump, ECA1, supports plant growth and confers tolerance to $Mn(^{2+})$ stress. *Plant Physiol.* **130**, 128–137 (2002).
24. R. F. Mills *et al.*, ECA3, a Golgi-localized P2A-type ATPase, plays a crucial role in manganese nutrition in Arabidopsis. *Plant Physiol.* **146**, 116–128 (2008).
25. X. Li *et al.*, A distinct endosomal Ca^{2+}/Mn^{2+} pump affects root growth through the secretory process. *Plant Physiol.* **147**, 1675–1689 (2008).
26. S. S. Conte *et al.*, *Arabidopsis thaliana* Yellow Stripe1-Like4 and Yellow Stripe1-Like6 localize to internal cellular membranes and are involved in metal ion homeostasis. *Front. Plant Sci.* **4**, 283 (2013).
27. A. Sasaki, N. Yamaji, J. Xia, J. F. Ma, OsYSL6 is involved in the detoxification of excess manganese in rice. *Plant Physiol.* **157**, 1832–1840 (2011).
28. S. Koike *et al.*, OsYSL2 is a rice metal-nicotianamine transporter that is regulated by iron and expressed in the phloem. *Plant J.* **39**, 415–424 (2004).
29. B. Zhang *et al.*, Inner envelope CHLOROPLAST MANGANESE TRANSPORTER 1 supports manganese homeostasis and phototrophic growth in Arabidopsis. *Mol. Plant* **11**, 943–954 (2018).
30. C. H. Yang *et al.*, Golgi-localised manganese transporter PML3 regulates Arabidopsis growth through modulating Golgi glycosylation and cell wall biosynthesis. *New Phytol.* **231**, 2200–2214 (2021).
31. A. Schneider *et al.*, The evolutionarily conserved protein PHOTOSYNTHESIS AFFECTED MUTANT71 is required for efficient manganese uptake at the thylakoid membrane in Arabidopsis. *Plant Cell* **28**, 892–910 (2016).
32. M. Eisenhut *et al.*, The plastid envelope CHLOROPLAST MANGANESE TRANSPORTER1 is essential for manganese homeostasis in Arabidopsis. *Mol. Plant* **11**, 955–969 (2018).
33. J. F. Shao, N. Yamaji, R. F. Shen, J. F. Ma, The key to Mn homeostasis in plants: Regulation of Mn transporters. *Trends Plant Sci.* **22**, 215–224 (2017).
34. J. Kudla *et al.*, Advances and current challenges in calcium signaling. *New Phytol.* **218**, 414–431 (2018).
35. Q. Dong, B. Bai, B. O. Almutairi, J. Kudla, Emerging roles of the CBL-CIPK calcium signaling network as key regulatory hub in plant nutrition. *J. Plant Physiol.* **257**, 153335 (2021).
36. T. Asano, N. Hayashi, S. Kikuchi, R. Ohsugi, CDPK-mediated abiotic stress signaling. *Plant Signal. Behav.* **7**, 817–821 (2012).
37. Z. Zhang *et al.*, Tonoplast-associated calcium signaling regulates manganese homeostasis in Arabidopsis. *Mol. Plant* **14**, 805–819 (2021).
38. C. Ju *et al.*, Ca^{2+}-dependent successive phosphorylation of vacuolar transporter MTP8 by CBL2/3-CIPK3/9/26 and CPK5 is critical for manganese homeostasis in Arabidopsis. *Mol. Plant* **15**, 419–437 (2022).
39. A. Schneider, Insights into manganese transport: A matter of phosphorylation. *Mol. Plant* **15**, 385–387 (2022).
40. J. He, N. Rössner, M. T. T. Hoang, S. Alejandro, E. Peiter, Transport, functions, and interaction of calcium and manganese in plant organellar compartments. *Plant Physiol.* **187**, 1940–1972 (2021).
41. G. Dubeaux, J. Neveu, E. Zelazny, G. Vert, Metal sensing by the IRT1 transporter-receptor orchestrates its own degradation and plant metal nutrition. *Mol. Cell* **69**, 953–964.e5 (2018).
42. L. Castaings, C. Alcon, T. Kosuth, D. Correia, C. Curie, Manganese triggers phosphorylation-mediated endocytosis of the Arabidopsis metal transporter NRAMP1. *Plant J.* **106**, 1328–1337 (2021).
43. A. Agorio *et al.*, Phosphatidylinositol 3-phosphate-binding protein AtPH1 controls the localization of the metal transporter NRAMP1 in *Arabidopsis*. *Proc. Natl. Acad. Sci. U.S.A.* **114**, E3354–E3363 (2017).
44. Q. Dong, L. Wallrad, B. O. Almutairi, J. Kudla, Ca^{2+} signaling in plant responses to abiotic stresses. *J. Integr. Plant Biol.* **64**, 287–300 (2022).
45. R. Waadt, M. Krebs, J. Kudla, K. Schumacher, Multiparameter imaging of calcium and abscisic acid and high-resolution quantitative calcium measurements using R-GECO1-mTurquoise in Arabidopsis. *New Phytol.* **216**, 303–320 (2017).
46. L. P. Hamel, J. Sheen, A. Séguin, Ancient signals: Comparative genomics of green plant CDPKs. *Trends Plant Sci.* **19**, 79–89 (2014).
47. M. Boudsocq, J. Sheen, CDPKs in immune and stress signaling. *Trends Plant Sci.* **18**, 30–40 (2013).
48. S. Y. Ma, W. H. Wu, AtCPK23 functions in Arabidopsis responses to drought and salt stresses. *Plant Mol. Biol.* **65**, 511–518 (2007).
49. S. Franz *et al.*, Calcium-dependent protein kinase CPK21 functions in abiotic stress response in *Arabidopsis thaliana*. *Mol. Plant* **4**, 83–96 (2011).
50. S. Shi *et al.*, The *Arabidopsis* calcium-dependent protein kinases (CDPKs) and their roles in plant growth regulation and abiotic stress responses. *Int. J. Mol. Sci.* **19**, 1900 (2018).
51. X. Chen *et al.*, Protein kinases in plant responses to drought, salt, and cold stress. *J. Integr. Plant Biol.* **63**, 53–78 (2021).
52. B. Zhang, C. Zhang, C. Liu, A. Fu, S. Luan, A Golgi-localized manganese transporter functions in pollen tube tip growth to control male fertility in *Arabidopsis*. *Plant Commun.* **2**, 100178 (2021).
53. F. Supek, L. Supekova, H. Nelson, N. Nelson, A yeast manganese transporter related to the macrophage protein involved in conferring resistance to mycobacteria. *Proc. Natl. Acad. Sci. U.S.A.* **93**, 5105–5110 (1996).
54. L. Sun *et al.*, Restriction of iron loading into developing seeds by a YABBY transcription factor safeguards successful reproduction in Arabidopsis. *Mol. Plant* **14**, 1624–1639 (2021).
55. C. Curie, J. M. Alonso, M. Le Jean, J. R. Ecker, J. F. Briat, Involvement of NRAMP1 from Arabidopsis thaliana in iron transport. *Biochem. J.* **347**, 749–755 (2000).
56. D. Geiger *et al.*, Guard cell anion channel SLAC1 is regulated by CDPK protein kinases with distinct Ca^{2+} affinities. *Proc. Natl. Acad. Sci. U.S.A.* **107**, 8023–8028 (2010).
57. P. J. M. van Kleeff *et al.*, The Arabidopsis GORK K^{+}-channel is phosphorylated by calcium-dependent protein kinase 21 (CPK21), which in turn is activated by 14-3-3 proteins. *Plant Physiol. Biochem.* **125**, 219–231 (2018).
58. T. Maierhofer *et al.*, Site- and kinase-specific phosphorylation-mediated activation of SLAC1, a guard cell anion channel stimulated by abscisic acid. *Sci. Signal.* **7**, ra86 (2014).
59. D. Geiger *et al.*, Stomatal closure by fast abscisic acid signaling is mediated by the guard cell anion channel SLAH3 and the receptor RCAR1. *Sci. Signal.* **4**, ra32 (2011).
60. S. Scherzer, T. Maierhofer, K. A. Al-Rasheid, D. Geiger, R. Hedrich, Multiple calcium-dependent kinases modulate ABA-activated guard cell anion channels. *Mol. Plant* **5**, 1409–1412 (2012).
61. F. L. Wang *et al.*, A potassium-sensing niche in Arabidopsis roots orchestrates signaling and adaptation responses to maintain nutrient homeostasis. *Dev. Cell* **56**, 781–794.e6 (2021).
62. S. Behera *et al.*, Two spatially and temporally distinct Ca^{2+} signals convey Arabidopsis thaliana responses to K^{+} deficiency. *New Phytol.* **213**, 739–750 (2017).
63. S. Behera *et al.*, Analyses of Ca^{2+} dynamics using a ubiquitin-10 promoter-driven Yellow Cameleon 3.6 indicator reveal reliable transgene expression and differences in cytoplasmic Ca^{2+} responses in Arabidopsis and rice (*Oryza sativa*) roots. *New Phytol.* **206**, 751–760 (2015).
64. R. Waadt, Live imaging of abscisic acid dynamics using genetically encoded fluorescence resonance energy transfer (FRET)-based ABA biosensors. *Methods Mol. Biol.* **2462**, 135–154 (2022).
65. M. Walter *et al.*, Visualization of protein interactions in living plant cells using bimolecular fluorescence complementation. *Plant J.* **40**, 428–438 (2004).
66. J. Kudla, R. Bock, Lighting the way to protein-protein interactions: Recommendations on best practices for bimolecular fluorescence complementation analyses. *Plant Cell* **28**, 1002–1008 (2016).
67. H. Su *et al.*, Abscisic acid signaling negatively regulates nitrate uptake via phosphorylation of NRT1.1 by SnRK2s in Arabidopsis. *J. Integr. Plant Biol.* **63**, 597–610 (2021).